

Oxygen vacancy-dependent chemical intermediates on Ru/MnO_x catalysts dictate the selectivity of CO₂ reduction

Hui Kang ^{a,b}, Lixuan Ma ^c, Shiyan Li ^{b,d}, Xingkun Chen ^e, Wei Chu ^{a,*}, Riguang Zhang ^{c,*}, Siglinda Perathoner ^f, Gabriele Centi ^f, Yuefeng Liu ^{b,*}

^a College of Chemical Engineering, Sichuan University, Chengdu 610065, China

^b Dalian National Laboratory for Clean Energy, Dalian Institute of Chemical Physics, Chinese Academy of Sciences, Dalian 116023, China

^c State Key Laboratory of Clean and Efficient Coal Utilization, College of Chemical Engineering and Technology, Taiyuan University of Technology, Taiyuan 030024, China

^d University of Chinese Academy of Sciences, Beijing 100049, China

^e Hangzhou Institute of Advanced studies, Zhejiang Normal University, Hangzhou 311231, China

^f Department of ChiBioFarAm, University of Messina, Messina 98166, Italy



ARTICLE INFO

Keywords:

CO₂ reduction
Catalytic selectivity
Formate intermediate
Surface oxygen vacancies
Manganese oxide

ABSTRACT

Structural dependence of the formation and transformation of the surface intermediates is the key to controlling the catalytic selectivity. Especially a highly controversial issue is whether formate species are spectator or active intermediates for CO₂ reduction. Herein, the Ru/MnO_x catalysts with different oxygen vacancy densities were developed to clarify these aspects. The high-defective RuMn-O_v showed high CH₄ selectivity (i.e. 89.3 % for CH₄ at 320 °C), while the low-defective RuMn-C mainly produced CO (i.e. 100 % for CO at 320 °C). By using multiple characterizations combined with theoretical modelling, it can be proved that the surface oxygen vacancies on MnO_x induces the generation of the formate intermediate, followed by hydrogenated to methane via spillover H derived from Ru nanoparticle. Remarkably, the RuMn-C catalyst at high Ru loading (c.a. 5 wt%) without formate intermediates achieved over 93 % CO selectivity. The results give an instructive way to understand the selectivity regulation driven by response reaction pathways.

1. Introduction

Selective hydrogenation of CO₂ is an important research topic that combines meeting carbon reduction targets, carbon circularity in the chemical industry, and valorization of the hydrogen economy by enabling efficient methods for chemical energy storage. The greenhouse gas CO₂ can be the storage carrier for H₂ produced with renewable energy sources, converting it into easily storable and transportable fuels or chemical raw materials such as methanol and syngas [1,2]. The primary products of CO₂ hydrogenation at atmospheric pressure are CH₄ and CO, with the former widely used as a fuel and basic chemical and the latter being the fundamental raw material in Fischer-Tropsch synthesis, methanol synthesis, and other fields. Achieving high selectivity for the target product can significantly reduce the separation costs, making it essential to unravel the relationship between catalytic structure and selectivity [3–6].

Heterogeneous catalysts exhibit multiple sites, with particular

emphasis often placed on the metal or metal-support interface as the pivotal factor governing reaction performance, which determines selective formation and transformation of intermediates (such as CO and formate, etc.) [7]. Typically, weakening the CO adsorption strength of metal in favour of promoting its rapid desorption can avoid the complete hydrogenation to methane. This tuning of the performances depends mainly on the active metal's electronic configuration and coordination geometry [2]. Various strategies, including i) reducing *d*-electron density [8], ii) decreasing the particle size [9,10], iii) varying the surface properties by strong metal-support interaction (SMSI) effect [11], and iv) making alloys [12], have been used to weaken the CO adsorption and enhance the CO selectivity. Even with these advances in designing the catalysts to control the selectivity in CO₂ reduction reactions, the mechanistic question of the factors triggering the selectivity from CO to CH₄ remains a matter of debate.

While the presence of the formate intermediate is frequently observed, ongoing debates persist regarding the structural factors

* Corresponding authors.

E-mail addresses: chuwei1965@scu.edu.cn (W. Chu), zhangriguang@tyut.edu.cn (R. Zhang), yuefeng.liu@dicp.ac.cn (Y. Liu).

influencing its formation and, thus, its effective role in determining the catalytic selectivity [8,13]. Wang et al. [14] reported that Ru/CeO₂ and Ru/Al₂O₃ went through different reaction pathway for CO₂ methanation. Ru/CeO₂ catalyst with formate intermediate exhibited higher methanation activity than Ru/Al₂O₃ with CO intermediate. However, other literature results are in contrast with this indication. Bobadilla et al. [15] compared CO₂ hydrogenation intermediates on Au/TiO₂ and Au/Al₂O₃ catalysts, exhibiting both 100 % CO selectivity. The formate predominantly formed on the non-reducible support Al₂O₃, while on Au/TiO₂, the reaction went through a redox mechanism with the formation of bicarbonate intermediates. Similarly, Rabee et al. [16] reported that the formate pathway was predominant on Au/ZrO₂ rather than Au/TiO₂. The preceding studies reveal a conspicuous discrepancy between the preferential generation of formate and the reducibility of the support. Meanwhile, it does not demonstrate the dependence of selectivity on the nature of the intermediate unambiguously.

Feng et al. [17] combined operando diffuse reflectance infrared Fourier transform spectroscopy (DRIFTS) results with density functional theory (DFT) calculations, indicating that the Zn-O-Zr asymmetry site is pivotal in formate formation and transformation to produce methanol. Dostagir et al. [18] reported that formate intermediates bridging Co and Zr sites form in CO₂ reduction to CO on Co-doped ZrO₂ (isolated Co ions). On the contrary, formate species at the interface between the Co nanoparticles and ZrO₂ support form when Co-nanoparticles are present, and this formate species converts to methane. Thus, the role of reducibility of the support or oxygen vacancies in the selective formation of intermediate is controversial. Moreover, oxygen vacancies may also contribute to CO₂ adsorption [19], H spillover [20], and interactions with metal [21], depending on distinct catalyst supports or metal active sites.

The intricate relationship between the structural characteristics and the resulting formate formation and its contradictory implications for reaction selectivity highlights a notable level of complexity. A source of uncertainty is that catalysts with different supports and types of surface metal nanoparticles are compared for different reactions in CO₂ hydrogenation (reverse water gas shift, methanol, or methane production). Therefore, there exists a need for a more precise understanding of the synergistic effect of various sites in heterogeneous catalysts that regulates the selective generation and conversion of intermediates by limiting the variability to a single factor.

Manganese oxide is a multivalent oxide with a highly adjustable surface structure, making it an excellent support for investigating the dependence of catalytic reactions on surface microstructure [22]. It was frequently used as a catalytic promoter for CO₂ methanation [23,24]. In this study, we synthesized Ru/MnO_x catalysts with distinct densities of oxygen vacancies in the MnO_x supports. They have comparable Ru nanoparticles and identical MnO_x crystal characteristics. High-defective RuMn-O_v (Ru/MnO_x-O_v) exhibits high CH₄ selectivity, whereas low-defective RuMn-C (Ru/MnO_x-C) has high CO selectivity. Thus, they are excellent candidates for a more precise comparison to understand the role of the synergistic effect of metal and support on catalytic selectivity.

In these highly active catalysts, we will prove that the metal Ru does not affect the types of adsorption intermediates. Its role is to dissociate H₂, generating H-spillover. The latter then diffuses to the support to CO₂ chemisorbed sites, where the CO₂ catalytic reduction occurs. The selective generation of intermediates mainly depends on the surface properties of MnO_x support and formate generated on MnO_x-O_v, while CO forms on MnO_x-C. The formate intermediate can be further hydrogenated to methane when spillover H generated by Ru nanoparticles is present. We thus proved, using a combination of multiple characterization and *in-situ* methods together with theoretical modelling, that the selectivity in CO₂ reduction is triggered by controlling the surface structure of the MnO support rather than by Ru nanoparticle characteristics and/or sites at the interface with the support. The generation of formate intermediate determined by the defects in MnO_x is the decisive

factor in forming methane as the final product. These findings are relevant for elucidating the CO₂ hydrogenation mechanism and advancing the development of highly selective catalysts.

2. Experimental section

2.1. Materials and chemicals

The following chemical reagents were used without further purification: Potassium permanganate (KMnO₄, 99.5 %, Tianjin Fangzheng Reagent factory), Manganese (II) acetate tetrahydrate (Mn (CH₃COO)₂·4H₂O, >99 %, Sinopharm), Manganese sulfate monohydrate (MnSO₄·H₂O, >99 %, Sinopharm), Ruthenium(III) nitrosyl nitrate solution (Ru(NO)(NO₃)_x(OH)_y, x+y=3, 1.5 % w v⁻¹, Macklin).

2.2. Synthesis of the catalysts and reference systems

The reflux method was used to synthesize MnO_x-C [25]. 200 ml deionized water and 0.64 g manganese sulfate monohydrate were added to a flask and heated to 80 °C. Meanwhile, 0.40 g potassium permanganate was added to a beaker containing 200 ml deionized water dissolved via ultrasound. Subsequently, the potassium permanganate solution was poured into the flask and vigorously stirred. The resulting mixture was then refluxed for 2 hours at 80 °C. Then, the suspension was filtered and washed with deionised water. Finally, the sample was dried overnight at 60 °C. The sample was then calcined at 450 °C for 3 hours (5 °C min⁻¹) to obtain the MnO_x-C carrier.

The MnO_x-O_v was synthesized by the precipitation method [26]. Briefly, a 50 ml 1 M manganese acetate aqueous solution was slowly added dropwise into 50 ml 1 M ammonium carbonate aqueous solution in a flask with vigorous stirring. The resulting suspension was stirred for another 4 hours followed by filtered and washed three times with deionized water. The filter cake was dried overnight at 60 °C and further calcined at 450 °C for 3 h (5 °C min⁻¹) to obtain the MnO_x-O_v carrier.

The wet impregnation method synthesized RuMn-M catalysts (equivalent to Ru/MnO_x-M, where M= C or O_v). For instance, in the preparation of a sample loaded with 0.5 wt% Ru, 0.995 g MnO_x carrier was mixed with 335 µl ruthenium (III) nitrosyl nitrate solution (1.5 % w·v⁻¹) in 30 ml deionized water under continuous stirring at room temperature for 1 hour. Then, the suspension was heated to 50 °C and stirred until no visible moisture was present. The resulting mixture was dried overnight at 60 °C and calcined at 350 °C for 3 hours (5 °C min⁻¹) to obtain the RuMn-M.

2.3. Characterization

X-ray powder diffraction (XRD) was used to analyze the crystalline structure of calcined and reduced samples on the X'pert-Pro diffractometer of Holland PANalytical, (Cu K α radiation, 40 kV, 40 mA). The loading of Ru of calcined catalysts was determined by inductively coupled plasma optical emission spectrometry (ICP) on the PerkinElmer 7300DV instrument. High-resolution (scanning) transmission electron microscope (S)TEM images were obtained on the JEM-2100 and probe-corrected JEM ARM200F electron microscope operating at 200 kV. The EDS line scanning was done on the energy-dispersive X-ray analyzer (EDX, EX-230 100 m² detector) equipped with the JEM ARM200F microscope. The EPR spectra were acquired using a Bruker A200 spectrometer for the reduced catalysts without exposure air. The surface element valence and content analysis were based on *nearly in-situ* XPS on ThermoFisher Escalab 250 Xi+ with monochromated Al K α radiation at a pass energy of 20 eV. The catalysts were pre-reduced in a hydrogen atmosphere at 500 °C for 1 hour, followed by vacuum transfer to XPS analysis. DRIFTS detected the adsorption and dissociation of reactants by catalysts on VERTEX 80 V (Bruker). The catalyst was pre-reduced at 500 °C for 1 h in H₂ and purged in Ar for 30 min. H₂ and Ar are highly pure, and the reacting gas was 5 %CO₂+15 %H₂+80 %Ar. Spectra were

obtained at intervals of 30 s by collecting 32 scans with a resolution of 4 cm⁻¹. H₂ temperature programmed reduction (H₂-TPR) and CO₂ temperature programmed desorption (CO₂-TPD) were carried out on AutoChem2920 of Micromeritics Instrument Corp. with a TCD detector. 100 mg catalyst was pretreated with 30 ml min⁻¹ Ar at 200 °C for 30 min to remove the surface adsorbent species and then ramped from 50 °C to 500 °C (10 °C min⁻¹) in 10 %H₂/Ar (50 ml min⁻¹), and the TCD signals were recorded to obtain H₂-TPR curves. The above catalyst was further reduced at 500 °C for 1 h and then switched to Ar for 30 min. After cooling to 50 °C, high-purity CO₂ was pre-adsorbed for 30 min, followed by 30 ml min⁻¹ He purged to baseline to stabilize. The CO₂-TPD curve was recorded with the temperature ramping from 50 °C to 700 °C (10 °C min⁻¹). The experimental procedure for H₂-TPD was similar to that of CO₂-TPD, except that CO₂ was replaced with 10 %H₂/Ar, the carrier gas He was replaced with Ar, and the MS signal of H₂ (*m/z*=2) was detected. CO+H₂ temperature programmed reaction (CO+H₂-TPR), HCOOH temperature programmed surface reaction (HCOOH-TPSR), and O₂-H₂ titration experiments were carried out on homemade fix-bed reaction equipment with an online gas mass spectrometer (Pfeiffer Vacuum). All catalysts (100 mg) were pre-reduced at 500 °C for 2 h in H₂. For CO+H₂-TPR experiments, a 30 ml min⁻¹ CO+H₂ flow was first fed for 1 h at 50 °C to purge the sample and allow the baseline to stabilize. The MS signals of *m/z*=28 and *m/z*=15 were used to record the consumption of CO and the formation of CH₄ with reaction temperature ramping from 50 °C to 600 °C (10 °C min⁻¹). For HCOOH-TPSR experiments, the first 30 ml min⁻¹ Ar was fed for 30 min, passing the flow through a formic acid solution in an ice bath, then the fed was switched to H₂/Ar to purge the catalyst for 1 h until baseline stabilization. The MS signal of *m/z*=15 was used to record the formation of CH₄ with reaction temperature ramping from 50 °C to 700 °C (10 °C/min). H₂-O₂ titration experiments: 30 ml min⁻¹ 5 %O₂/He was pre-adsorbed at 50 °C for 60 min, then switched to 5 %H₂/Ar for 60 min to the baseline to stabilize. The MS signals of *m/z*=2 and *m/z*=18 were used to record the consumption of H₂ and the formation of H₂O with reaction temperature increasing from 50 °C to 600 °C at a rate of 10 °C min⁻¹.

2.4. Catalytic performance evaluation

The catalytic performances were performed in a fixed-bed reactor (quartz, inner diameter 8 mm). The influence of internal and external diffusion was excluded (Fig. S1) by a proper choice of the particle size of the catalyst (40–60 mesh) and the flow rate of reaction gas (100 ml min⁻¹). Calculations and tests confirmed the absence of these limitations. The catalyst was pre-reduced at 500 °C for 2 h in H₂. The reaction products were analyzed by Agilent gas chromatography (7820A) with a TCD detector. The CO₂ conversion (X_{CO_2}), CO selectivity (S_{CO}), and CO formation rates were calculated as follows:

$$X_{CO_2} = \frac{F_{CO_2,in} - F_{CO_2,out}}{F_{CO_2,in}} \times 100\% \quad (1)$$

$$S_{CO} = \frac{F_{CO,out}}{F_{CO_2,in} - F_{CO_2,out}} \times 100\% \quad (2)$$

$$Rate \quad (mmol \cdot g_{cat.}^{-1} \cdot h^{-1}) = \frac{F_{CO,out}}{m} \quad (3)$$

2.5. DFT calculation

Spin-polarized density functional theory calculations were carried out to examine the activation of CO₂ and the formation of formate species on the MnO-C and MnO-O_v catalysts. All the simulations were performed using the projector-augmented-wave method within the Vienna Ab-initio Simulation Package (VASP 5.4.4). The Perdew-Burke-Ernzerhof (PBE) approximation was used to account for exchange and correlation via a standard generalized gradient approximation (GGA). A

7×7×7 and 3×3×1 k-points sampling based on the Monkhorst-Pack scheme was used for bulk and surface optimization. A cut-off energy of 520 eV was used for all calculations. For all calculations, the initial magnetic moments of Mn²⁺ cations were configured to follow the AFM-II antiferromagnetic arrangement in bulk MnO. For geometric optimization, the forces and energy were minimized to less than 0.03 eV/Å and 10⁻⁵ eV, respectively. In order to account for the strongly localization of Mn 3d electrons of MnO-C and MnO-O_v catalysts, a Hubbard-like U term was used, (GGA+U), an effective parameter U-J=3.9 eV was set for Mn atom.

The adsorption energy (G_{ads}) were determined by the following equation:

$$G_{ads} = G_{surf+mol} - G_{surf} - G_{mol} \quad (4)$$

where $G_{surf+mol}$, G_{surf} and G_{mol} were the total free energies of the adsorbed system, the clean surface, and the free molecules, respectively. Considering the optimal catalytic reaction condition were 400 °C and 0.1 MPa, thus, the free and adsorbed molecules were corrected at 673 K and 1.0 MPa using VASPKIT tool in calculations [27]. In consideration of the determinant role of surface oxygen vacancies in the formation of formate species, the cubic MnO crystal with the space group of Fm-3 m is chosen as the theoretical calculation model (Fig. S2a). The calculated lattice parameters of bulk MnO are $a=b=c=4.436$ Å, which are close to the theoretical and experimental values in the literature [28,29]. Moreover, as shown in Fig. S2b and S2c, the perfect and defective MnO (220) surfaces without or with an oxygen vacancy are constructed based on the experimental results, labeled as, respectively. Both the MnO-C and MnO-O_v are used to provide a slab with a *p*(2×3) surface cell and a thickness of 3 at. layers along. A 15 Å vacuum gap was introduced after the optimization of the bulk structure. The bottom layer was fixed in their bulk and the top two layers were allowed to relax for surface geometry optimization.

3. Results and discussion

3.1. Structure and surface oxygen vacancies

Ru/MnO_x catalysts with different surface densities of oxygen vacancies were prepared. They were indicated as RuMn-C and RuMn-O_v where the first corresponds to a nearly clean surface and the second to high density of surface oxygen vacancies. They were synthesised using defined preparation procedures [25,26] (Fig. S3). The theoretical Ru loading of both RuMn-C and RuMn-O_v was 0.5 wt%. The actual Ru loading is shown in Table S1. The catalysts show near-spherical nanograins with similar MnO crystal structures (PDF #06-0592) [25] after reduction (Figs. S4 and S5). However, RuMn-C and RuMn-O_v show different concentrations of oxygen vacancies. Electron paramagnetic resonance (EPR) detects unpaired electrons in the materials, while both Mn²⁺ [30] and oxygen vacancy [22] contributed to the EPR signal. Stronger EPR intensity for the RuMn-O_v indeed possesses a higher density of oxygen vacancies (Fig. 1a).

Furthermore, nearly *in-situ* X-ray photoelectron spectroscopy (XPS) was used to analyse the surface chemical state of the reduced catalyst (Fig. S6). The electron binding energy of the Ru 3d_{5/2} spectrum in the RuMn-O_v catalyst was 0.4 eV higher than that of the RuMn-C catalyst (Fig. S6a), implying its relative electron deficiency (Ru^{δ+}). This shift is due to the strong interaction between the Ru and oxygen vacancies [21].

The presence of oxygen vacancies is further proven by the magnitude of peak splitting of Mn 3 s spectra, which is diagnostic of the Mn oxidation state [31]. The Mn 3 s spectra of RuMn-C and RuMn-O_v were the same with 6.0 eV multiplet splitting of Mn²⁺ (MnO) (Fig. S6b). However, upon normalising the Mn 2p spectra of both catalysts and subsequently generating differential spectra, an additional peak at approximately 640.1 eV was observed in the RuMn-O_v (Fig. 1b, top). This distinctive feature is attributable to Mn^{2-x} species formed due to the

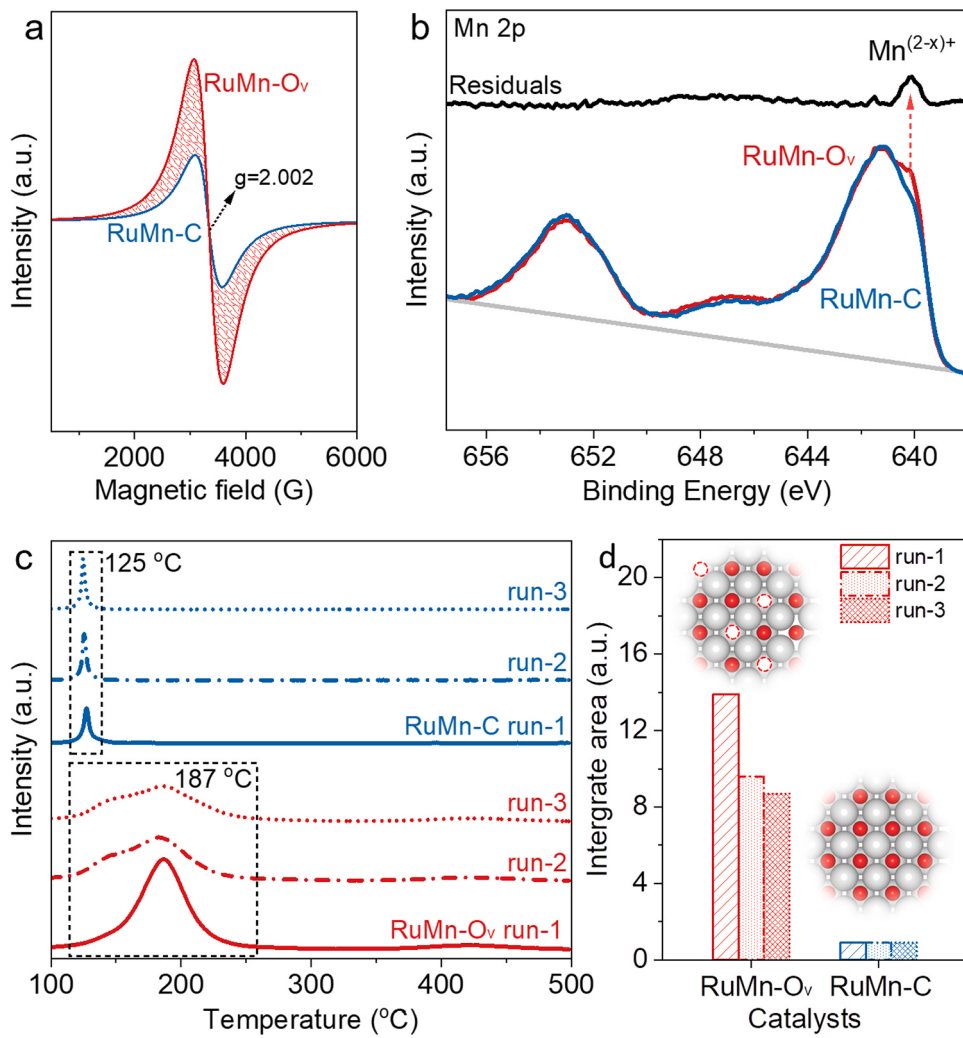


Fig. 1. Comparison of surface oxygen affinity for RuMn-O_v and RuMn-C catalysts. (a) Nearly *in-situ* EPR spectra of the reduced RuMn-O_v and RuMn-C. (b) Normalised Mn 2p spectra (nearly *in-situ* XPS) of RuMn-C and RuMn-O_v catalysts with their difference spectra on the top (black line, residuals). (c) Temperature programmed profiles, and (d) integrated area of H₂-O₂ titration experiments.

formation of oxygen vacancies. Meanwhile, the RuMn-O_v catalyst possessed a lower surface O/Mn ratio (lower than 1) than the RuMn-C catalyst (Fig. S7 and Supplementary Note 1). These findings provided conclusive evidence that RuMn-O_v had a notably higher density of surface oxygen vacancies.

The oxygen adsorption capacity (oxygen affinity) could be used to quantify the surface density of the oxygen vacancies [30,32]. RuMn-C and RuMn-O_v catalysts possessed similar reducibility based on the H₂ temperature programmed reduction (H₂-TPR) results with an almost overlapping reduction peak at 193 °C (Fig. S8a), attributing to the reduction of Mn⁴⁺→(Mn³⁺)→Mn²⁺ [33]. Meanwhile, the presented nearly identical H₂ consumption (Fig. S8b) indicating that oxygen vacancies originated from the catalyst surface. Cyclic H₂-O₂ titration experiments (repeated three times in sequence) were used to quantitatively assess the amount of oxygen vacancies. The methodology involves oxygen pre-adsorption at 50 °C (which coordinates at oxygen vacancies) followed by programmed temperature ramping in H₂. The maximum H₂ consumption peaks of RuMn-O_v were at 187 °C during the three cyclic experiments, e.g., higher than the corresponding peak in RuMn-C (around 125 °C) (Fig. 1c). The adsorption capacity of RuMn-O_v was 10–15 times higher than that of RuMn-C. This is quantified by integrating the H₂ consumption peaks (Fig. 1d). Additionally, the catalysts' oxygen affinity was demonstrated by the colour changes upon exposure to air after reduction (Fig. S9). After the reduction process, the

colour of the catalysts changes from black (MnO₂) to green (MnO). Then, the RuMn-O_v changed to brown within 2 minutes in the air, whereas most RuMn-C remained green even after being exposed to air for 60 minutes.

The average particle size of Ru on RuMn-O_v was about 1.0 nm, while that on RuMn-C was 2.2 nm, according to the statistical analysis of the transmission electron microscope results (Fig. 2). Both catalysts mainly exposed [220] and [111] crystal planes. The two catalysts show the same crystal nanostructure with identical exposed crystal facets. Therefore, the higher dispersion of Ru on RuMn-O_v due to oxygen vacancies [34]. The above characterisation data evidence that the two RuMn catalysts have a similar crystal structure of the support but different surface oxygen vacancy densities. The latter induces a slightly higher dispersion of Ru nanoparticles but does not affect their nano-morphology. Thus, these samples are well-defined catalysts for understanding the role of MnO_x support and oxygen vacancies in influencing the performances in CO₂ catalytic methanation.

3.2. Performances in CO₂ catalytic reduction

The behaviour of RuMn-C and RuMn-O_v catalysts in CO₂ thermal reduction is shown in Fig. 3a. Tests were performed in conditions that avoid internal and external diffusional limitations (Fig. S1). The RuMn-C catalyst showed nearly 100 % CO selectivity in the reaction temperature

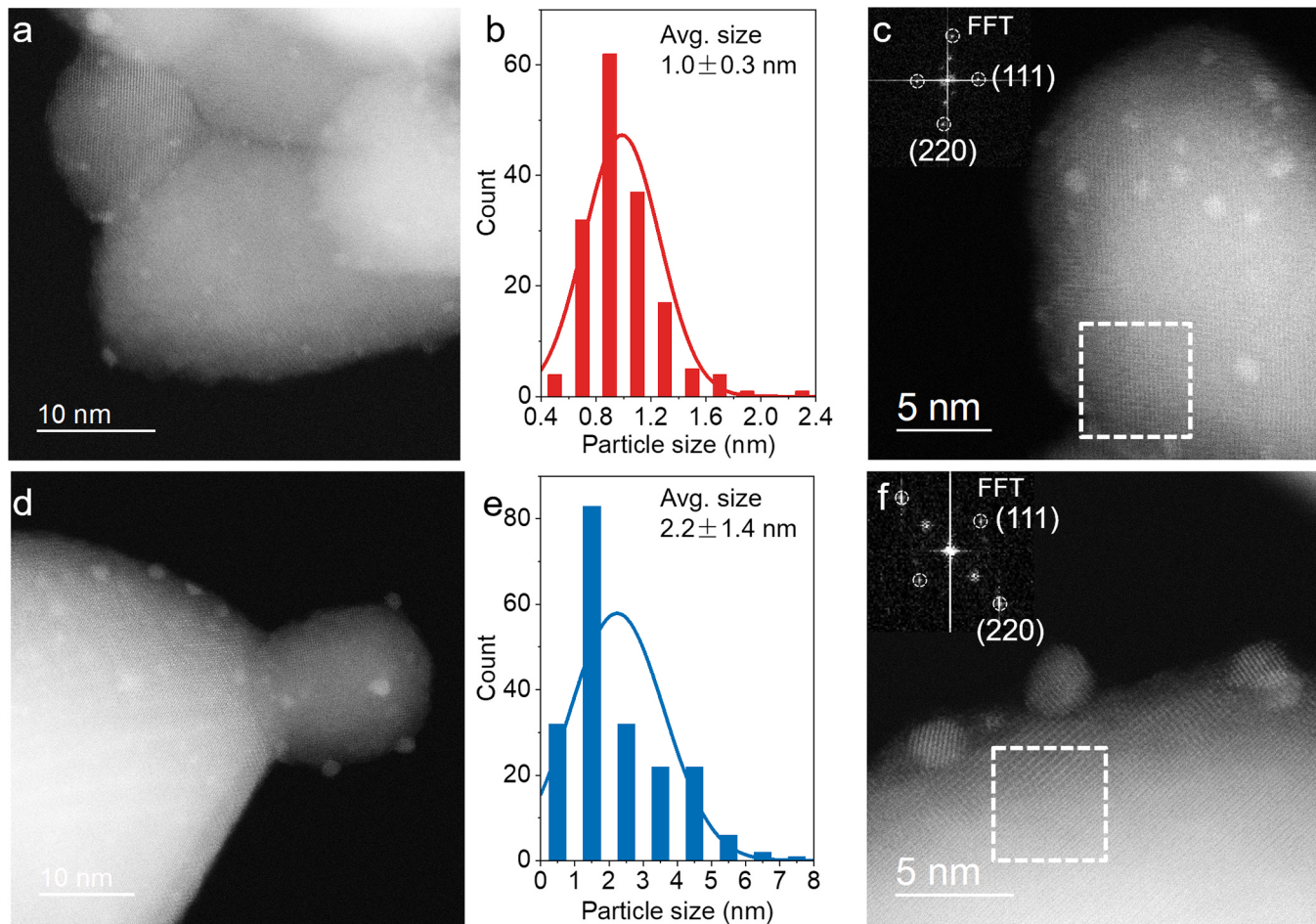


Fig. 2. High angle annular dark field scanning transmission electron microscope (HAADF-STEM) images and statistic Ru nanoparticle size distribution of (a-c) reduced RuMn-O_v and (d-f) reduced RuMn-C.

range of 320–500 °C, while the RuMn-O_v catalyst had significantly lower CO selectivity, less than 10 % below 400 °C. The increased CO selectivity above 400 °C for the RuMn-O_v catalyst is mainly due to the thermodynamic factor that high reaction temperature favours the reverse water gas shift (RWGS) reaction [35].

By increasing the WHSV (weight hourly space velocity) to 240,000 ml g⁻¹ h⁻¹ to have a CO₂ conversion <10 % for both catalysts (Fig. S10), RuMn-C still maintained 100 % CO selectivity, while RuMn-O_v showed high CH₄ selectivity (61.9 %) at 320 °C. The RuMn-O_v had better CO₂ hydrogenation activity, even if its activation energy (84.6 kJ mol⁻¹ for methanation) was higher than that of RuMn-C (71.9 kJ mol⁻¹ for RWGS) (Fig. S11). Thus, the improved activity is due to the higher pre-exponential factor, e.g., a higher number of active sites [4,36]. Surprisingly, ultra-high CO selectivity was obtained on the RuMn-C catalyst when the Ru loading increased from 0.5 % to 5.0 % wt. (CO selectivity > 93 %).

Ru is known as an excellent methanation catalyst due to its strong C–O bond dissociation ability [37,38]. Thus, increasing Ru loading is expected to decrease CO selectivity. The results in Fig. 3b and S12–S14 are the first evidence, to our knowledge, that dominant CO formation was archived over such a high-loading-content Ru-based catalyst (Table S2) [8,37,39]. Therefore, the selective behavior in these catalysts is not directly related to Ru nanoparticles as the active sites. Unlike our samples, inactive or poorly reactive supports were often used in CO₂ reduction catalysts. This indication is further supported by tests using Ni rather than Ru as a metal component (2 % loading on MnO_x-O_v and MnO_x-C support). The results of the catalytic tests show very different selectivity (91.5 % of CH₄ for 2%NiMn-O_v and 100 % of CO for 2%

NiMn-C at 400 °C, Fig. 3b). It should be noted that metallic Ni is considered an excellent catalyst for CO₂ methanation in the literature [40].

Increasing H₂ partial pressure is beneficial to hydrogenate further the reaction intermediates to form CH₄, resulting in lower CO selectivity [41]. However, the CO selectivity of the RuMn-C catalyst was not significantly affected by the H₂:CO₂. Even if H₂:CO₂ was increased to 6:1, the CO selectivity remained at 94.6 % (Fig. 3c). In contrast, the CO selectivity of the RuMn-O_v catalyst decreased as the H₂:CO₂ ratio increased. This result indicated that the two catalysts followed different reaction pathways.

In addition, long-term high-temperature reactions might also result in a decrease in CO selectivity due to the particle sintering [42]. The two catalysts maintain significant selectivity differences after the reaction at 400 °C for 48 h, although the CO₂ conversion slightly decreased, especially at the initial stage within 10 h (Fig. S15).

Further catalytic tests were conducted to demonstrate the differences in the two catalysts' intrinsic surface catalytic pathways by evaluating the CO hydrogenation performance. This reaction would indicate the role of CO as an intermediate to methane [4,42,43]. Higher H₂ partial pressure should positively shift CO methanation reaction equilibrium and increase the reaction rate. However, methane formation is not promoted even up to an H₂:CO ratio 18 (Fig. 3d). Therefore, in our catalysts, CO is not an intermediate in the pathway to methane.

CO₂+H₂ and CO+H₂ temperature programmed reaction results of RuMn-O_v were compared in Fig. 3e to obtain further mechanistic indications. The light-off temperature of CO methanation was about 68 °C higher than that of CO₂ methanation, and the former reaction rate was

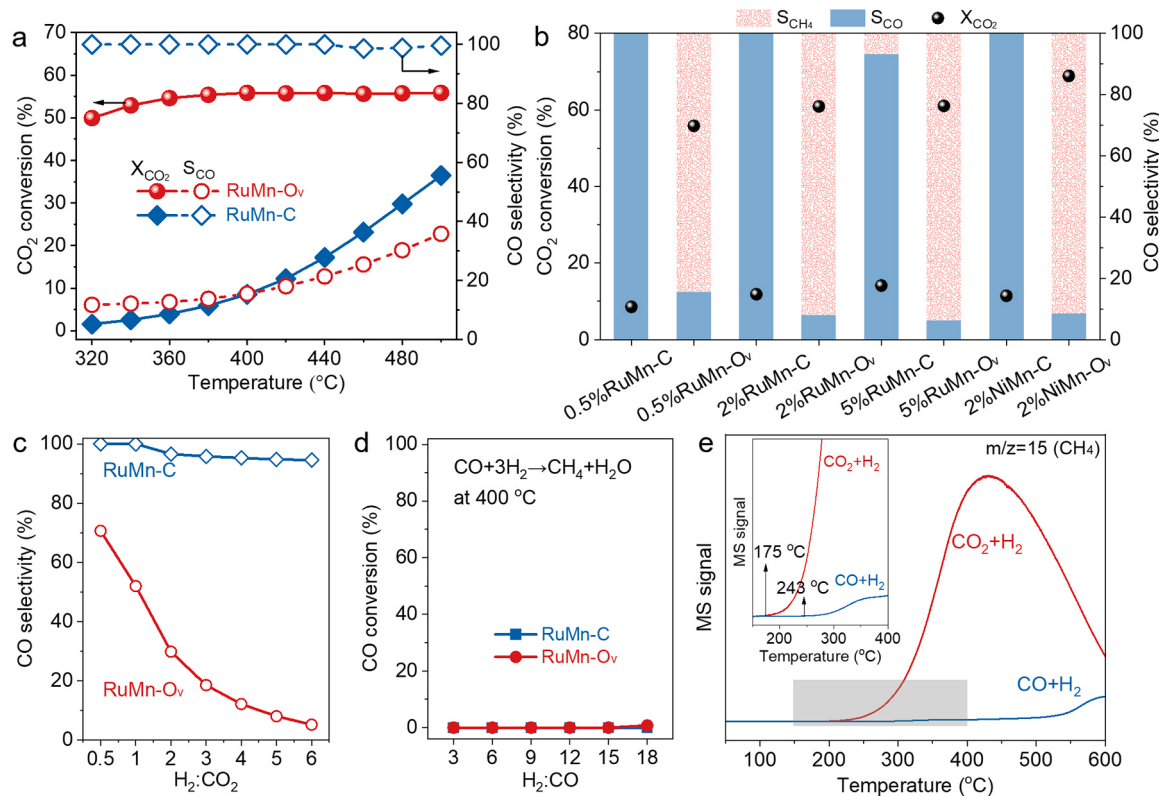


Fig. 3. Catalytic performance and temperature programmed experiments. (a) Temperature programmed CO₂ reduction activities of RuMn-O_v and RuMn-C catalysts. (b) CO₂ reduction performances of MMn-C and MMn-O_v (M=Ru or Ni) catalysts at 400 °C. (c) The H₂:CO₂ ratio effect on CO selectivity at 400 °C. Reaction condition: 100 mg catalyst, CO₂ (12 ml min⁻¹), H₂ (6–72 ml min⁻¹), N₂ as equilibrium gas ensured a total flow of 100 ml min⁻¹. (d) CO hydrogenation activity with varied H₂:CO ratio. Reaction condition: 100 mg catalyst, CO (5 ml min⁻¹), H₂ (15–90 ml min⁻¹), N₂ as equilibrium gas ensured a total flow of 100 ml min⁻¹. (e) CO₂+H₂-TPR and CO+H₂-TPR over RuMn-O_v catalyst, the inset was the local magnification for the grey region.

far lower than that of the latter by comparing the slope. It showed that the energy barrier of CO methanation was much higher than that of CO₂ methanation, indicating that CO was not the key intermediate in the methanation process of the RuMn-O_v catalyst [42].

3.3. Influence of Ru nanoparticles on the selectivity

It is widely accepted that Ru nanoparticles with a smaller size have a weaker CO adsorption ability, determining a faster carbon monoxide desorption and higher CO selectivity. Although the Ru nanoparticle size in RuMn-C and RuMn-O_v catalysts is comparable, the former shows an average size of 2.2 nm compared to 1.0 nm of RuMn-O_v (Fig. 2). If Ru nanoparticles determine the selective behavior, RuMn-C, with a larger average Ru particle size, should show a lower selectivity to CO, while they exhibited an exceptional selectivity of nearly 100 % towards CO in CO₂ hydrogenation.

Increasing the Ru loading content to 5 wt%, the average particle size of Ru on 5%RuMn-O_v increased to 2.1 nm, and that on 5%RuMn-C reached 3.7 nm (Fig. S16). These results indicate that Ru particle size did not directly influence the reaction selectivity (Fig. 3b). In addition, modifying the electronic state of a metal to form an electron-deficient center (M^{δ+}) could inhibit π back-donation and weaken the adsorption of CO [2], resulting in higher CO selectivity [4,44,45]. However, the RuMn-O_v catalyst with lower Ru electron density (in presence of Ru^{δ+}) displayed higher CH₄ selectivity, as shown in Fig. S6a and Fig. 3, indicating that the electronic state of Ru was also not the key factor affecting CO₂ selectivity.

In recent years, it has also been reported that strong metal-support interaction (SMSI) between VIII-group metals and reducible supports benefited the hydrogenation of CO₂ to CO [11,46]. Due to the SMSI effect, the reducible support migrated to the metal surface to form an

encapsulation structure of the metal nanoparticle, inhibiting the adsorption of small molecules such as CO and H₂ [47]. However, characterization data do not show Mn species over the surface of Ru nanoparticles (see results of energy dispersive spectroscopy EDS-linear scanning, Fig. S17). This result shows that the high CO selectivity of the RuMn-C catalyst was independent of the SMSI effect.

These results prove that the Ru nanoparticles are not directly involved in determining the selectivity and activity in CO₂ methanation of our RuMn_x catalysts. Nevertheless, the activity is much lower without Ru nanoparticles, as discussed later. The explanation is that Ru nanoparticles participate in the mechanism, not directly hosting the active sites for CO₂ chemisorption/ transformation but activating H₂. These Ru nanoparticles generate spillover hydrogen, which then migrate over the oxide to hydrogenate the intermediate species formed at support sites [36].

In conclusion, these and previous results in the catalytic CO₂ reduction unambiguously demonstrate that (i) sites on the support rather than on Ru nanoparticles are the active ones in CO₂ reduction; however, Ru nanoparticles play a role in generating spillover hydrogen; (ii) CO is not an intermediate in our case to methane, but CO and CH₄ form along two different pathways; (iii) the presence of oxygen vacancies in the Mn_x support is the factor triggering the surface pathways and selectivity.

We should comment that these RuMn catalysts are highly performant for CO₂ reduction, as shown in Table S2 comparing the results with literature data. Therefore, these catalysts are representative samples for CO₂ reduction, and related mechanistic indications are relevant. Mechanistic studies in the CO₂ reduction over these catalysts will provide further insights.

3.4. The role of oxygen vacancies on the selectivity

In-situ diffuse reflection Fourier infrared spectroscopy (DRIFTS) experiments were used to analyse the differences in the reaction pathways and surface intermediates on these catalysts. The results for RuMn-C in a feed of CO_2+H_2 at increasing reaction temperature from 50 to 350 °C are shown in Fig. S18 and Fig. 4a. No gaseous CH_4 was observed during the DRIFTS test on the RuMn-C catalyst (Fig. S18), which agrees with the catalytic data. The vibration strength of bridge adsorption CO (CO_{bri}) decreased with the temperature, while the linear adsorption CO (CO_{lin}) and weak gaseous CO appeared at 150 °C. The IR vibrational spectra of

CO_2 adsorption species were mainly in the 1000–1800 cm^{-1} range (Fig. 4a). Two adsorption intermediates were present on RuMn-C catalyst at 50 °C, which can be attributed to carboxylate [(i), 1667 and 1199 cm^{-1}] and bidentate carbonate [(ii), 1541, 1308, and 1047 cm^{-1}] respectively [48]. The intensity of carboxylate species showed a downward trend, especially at 150 °C, and the signal disappeared almost completely at 350 °C. In contrast, the bidentate carbonate signal intensity slightly increases during temperature ramping. The carboxylate consumption and CO formation strongly correlate, indicating that carboxylate was the key intermediate for RWGS reaction over the RuMn-C catalyst.

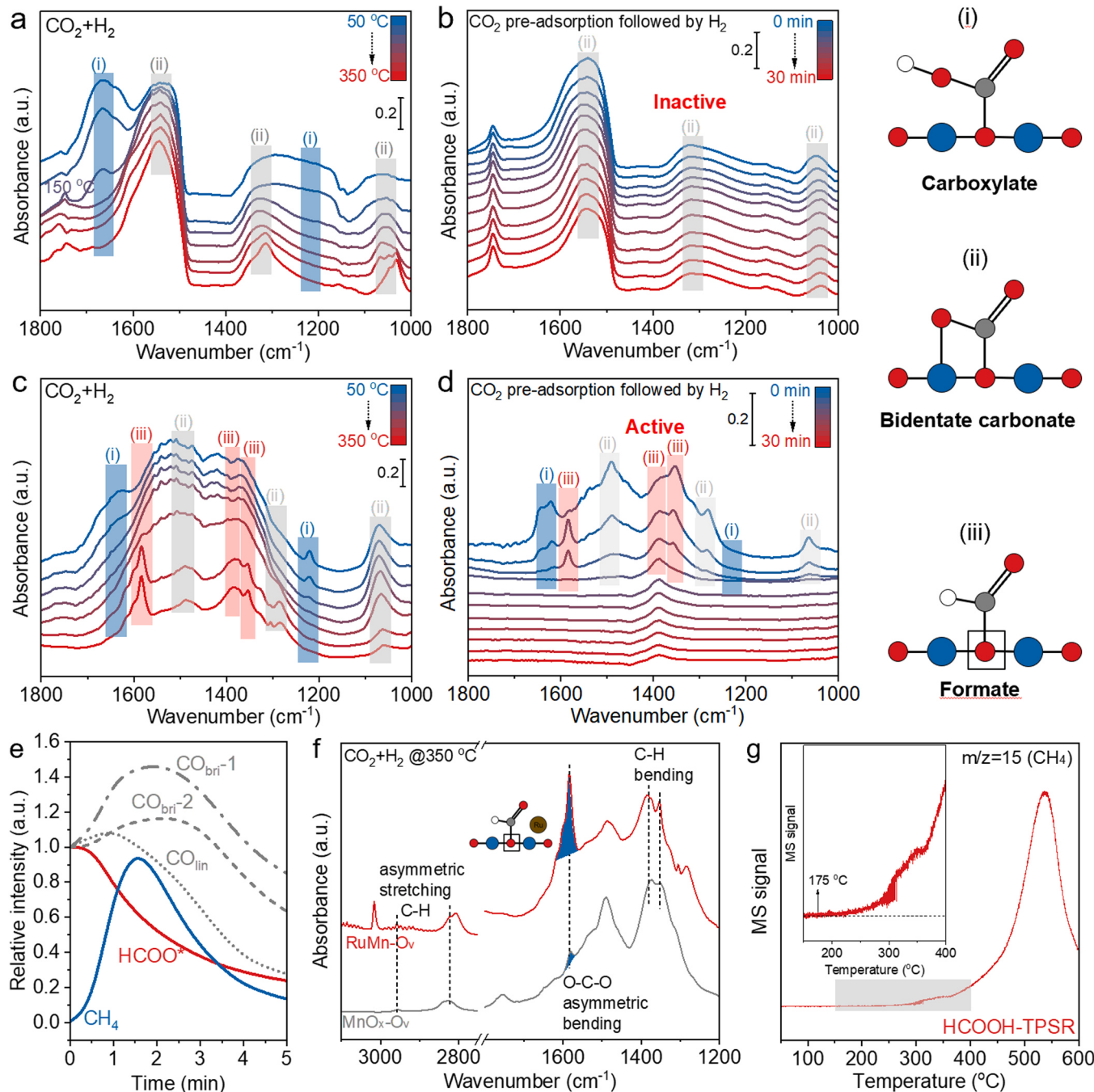


Fig. 4. Temperature-programmed CO_2+H_2 -DRIFTS ramping from 50 to 350 °C over (a) RuMn-C and (c) RuMn-Ov. Transient H_2 -DRIFTS after CO_2 pre-adsorption for 30 min at 350 °C over (b) RuMn-C and (d) RuMn-Ov. Scheme of (i) Carboxylate, (ii) Bidentate carbonate, and (iii) Formate. (e) The surface formate (HCOO^* , 1386 cm^{-1}), bridging CO adsorption ($\text{CO}_{\text{bri-1}}$, 1886 and $\text{CO}_{\text{bri-2}}$, 1934 cm^{-1}), linear CO (CO_{lin} , 2005–1959 cm^{-1}), and methane (3016 cm^{-1}) species versus time during the H_2 purging for CO_2 -preadsorbed RuMn-Ov catalyst. (f) Comparison of formate intermediate between RuMn-Ov and MnOx-Ov at 30 °C. (g) HCOOH pre-adsorption followed by H_2 temperature programmed surface reaction (HCOOH-TPSR).

The transient H₂-DRIFTS was further used to analyse the reactivity of surface intermediates (Fig. 4b and Fig. S19). The reduced RuMn-C catalyst preadsorbed CO₂ followed by H₂ purging at 350 °C. The bidentate carbonate was the only intermediate, and its signal intensity slightly decreased during the H₂ purging. These results indicate that the bidentate carbonate was an inactive species. Therefore, the reaction mechanism of hydrogenation of CO₂ to CO over the RuMn-C catalyst can be summarised as follows: (1) CO₂ was first adsorbed on the hydroxyl groups on the surface of the RuMn-C catalyst to form carboxylate and (2) then the carboxylate was further decomposed into product CO [49] with the bidentate carbonate as a spectator.

The RuMn-O_v catalyst showed more complex surface intermediates. The formate species [(iii), 1593, 1403, and 1375 cm⁻¹] was present besides carboxylate and bidentate carbonate (Fig. 4c and S20). The 1593 cm⁻¹ signal corresponds to the asymmetric vibration of formate, while the 1403 cm⁻¹ and 1375 cm⁻¹ signals correspond to the symmetric vibration [50]. During the temperature increase, the carboxylate species gradually decrease with a parallel formation of CO, similar to the RuMn-C catalyst. In contrast, the bidentate carbonate (a spectator for RuMn-C catalyst) decreased with increasing temperature, while the formate species increased in intensity and accumulated on the catalyst surface. The formate species are derived from the hydrogenation of carbon-contained surface-adsorbed species [49]. The three intermediates coexisted after CO₂ pre-adsorption (Fig. 4d and S21). However, they were all rapidly consumed in H₂ purging within 4 min from the start, forming CH₄. Therefore, adsorbed species on the surface of RuMn-O_v had more reactivity than over RuMn-C because they were all further hydrogenated to formate and eventually completely converted.

The enhanced CO₂ adsorption over RuMn-O_v was an important reason for formate formation [16]. Ye et al. [51] found that the oxygen affinity of the catalyst was beneficial to the enhancement of CO₂ adsorption by DFT calculation. RuMn-C catalyst had two adsorption peaks at 97 and 171 °C in CO₂ temperature programmed desorption (CO₂-TPD) shown in Fig. S22. The former was assigned to physical adsorption, and the latter was chemical adsorption. RuMn-O_v had a strongly enhanced CO₂ desorption peak at about 177 °C. The stronger CO₂ adsorption on RuMn-O_v due to surface oxygen vacancies might also change the intrinsic reactivity of the adspecies, leading to the formation of CH₄.

In addition, large amounts of adsorbed CO species are present on the RuMn-O_v catalyst (Fig. S21), which might come from the decomposition of partial carboxylate and formate [52]. The adsorption peak of linearly coordinated CO (CO_{lin}) quickly decreased when purging with H₂. It has been proved that CO was not the key intermediate for the methanation of the RuMn-O_v catalyst (Fig. 3d-e). Therefore, the decrease in the adsorption peak of CO_{lin} was mainly caused by desorption. DRIFTS results of CO pre-adsorption followed by Ar purging are shown in Fig. S23. The CO_{lin} adsorption peak also showed a similar declining trend. This result revealed the small amount of CO produced during CO₂ hydrogenation activity testing (see results in Fig. 3b).

Based on the above DRIFTS results, it may be indicated that generating formate on the surface of the RuMn-O_v catalyst was a critical factor contributing to its high selectivity towards CH₄. The hypothesis could be further verified by quantitatively analysing the variation of the surface species on the RuMn-O_v catalyst based on the data from Fig. 4d and Fig. S21. The normalised absorbance of surface formate (HCOO*, 1386 cm⁻¹), bridging CO adsorption (CO_{bri-1}, 1886 and CO_{bri-2}, 1934 cm⁻¹), linear CO (CO_{lin}, 2005–1959 cm⁻¹), and methane (3016 cm⁻¹) species versus time during H₂ purging after CO₂ adsorption is shown in Fig. 4e. A noteworthy finding was the significant negative correlation between methane production and formate consumption in first 1.5 min, while CO species exhibited an initial increase followed by a subsequent decrease. The bridging-adsorption CO with higher reactivity was predominantly retained within 5 min, whereas the weak adsorption of linear CO was removed by purging. This trend indicates that the

formate acts as the highly active intermediate in forming CH₄ over the RuMn-O_v catalyst rather than the CO intermediate. Their disappearance rate should increase linearly with their surface concentration by assuming a first-order dependence from the concentration of the adsorbed formate species. However, DRIFTS data indicate a higher rate, also normalising the concentration of adspecies. Thus, the intrinsic rate enhancement is related to the higher concentration of oxygen vacancies in comparing the results of the two catalysts.

Notably, the formate formation could also occur on the MnO_x-O_v support without Ru-loaded [53] (Fig. 4f and S24), indicating that formate formation was independent of the metal or metal-support interface. However, the MnO_x-O_v support possessed nearly 100 % CO selectivity (Fig. S25). This result was consistent with literature reporting that surface formate species located away from the active metal nanoparticles can be dehydrogenated to CO [4,54]. The RuMn-O_v catalyst presented a significantly enhanced O-C-O asymmetric bending compared with MnO_x-O_v without an obvious peak shift (Fig. 4f). It indicated that Ru nanoparticles may promote the formate formation. The interpretation is that this species is a surface CO₂ chemisorbed species interacting with spillover hydrogen. It is thus an intermediate to formate, which further hydrogenates to CH₄. Furthermore, the CH₄ was observed over RuMn-C during HCOOH pre-adsorption followed by H₂ temperature programmed surface reaction (HCOOH-TPSR) (Fig. 4g). These DRIFTS and HCOOH-TPSR results thus show that formate generation depends on the support's high oxygen vacancy and spillover H (generated at Ru nanoparticles), which induce the further hydrogenation of formates to methane.

3.5. Theoretical support to mechanistic indications

Based on the above discussion, surface vacancies in MnO emerge as the pivotal determinant for forming formate species. This assertion is further substantiated through density functional theory (DFT) (Figs. S26–S28 and 5a-b, Tables S3–S4). Two cubic MnO surface models (MnO-C and MnO-O_v) were constructed with or without an oxygen vacancy, respectively (Fig. S25). The stable adsorption models in DFT calculations were optimized for all involved C-containing species (CO₂, COOH, etc.) on MnO-C and MnO-O_v surface. The adsorption energy of formate over MnO-O_v was higher than that over MnO-C (-364.2 vs. -216.2 kJ mol⁻¹), which would promote the formation of the HCOO* intermediate (Table S3). Furthermore, the possible formation pathway of formate was analysed, as shown in Figs. 5a-b. Over MnO-C, both the generation of HCOO* and COOH* species from CO₂ hydrogenation displayed exceptionally high activation barriers (192.9 and 142.9 kJ mol⁻¹, respectively). Over MnO-O_v, the formate species (HCOO*) derived from adsorbed COOH* has a significantly lower activation energy barrier than the direct hydrogenation of CO₂ to form HCOO* species (53.6 vs 161.6 kJ mol⁻¹). In the latter, the rate-determining step of HCOOH* formation is CO₂*+H*→COOH* with the activation barrier and reaction energy of 41.5 and 18.9 kJ mol⁻¹. This observation implies that forming formate species on the pristine surface is virtually negligible, in agreement with the DRIFTS results (Fig. 4). Therefore, the surface oxygen vacancy induces the formate generation and a change in their intrinsic reactivity, in agreement with the experimental results and related interpretation.

3.6. Metal Ru and MnO synergy through H-spillover

The enhanced H spillover facilitates the hydrogenation of CO₂ [55], as commented before. The surface oxygen vacancies promote the generation of surface hydroxyl groups, which act as active sites for enhancing CO₂ chemisorption and facilitating H spillover mobility [56].

H-D isotope exchange DRIFTS experiments further prove these results (Fig. S29). The stronger O-D and O-H vibration peaks observed over RuMn-O_v indicate a superior H spillover ability in comparison to RuMn-C. Additionally, the similarly weak H-D exchange DRIFTS intensities

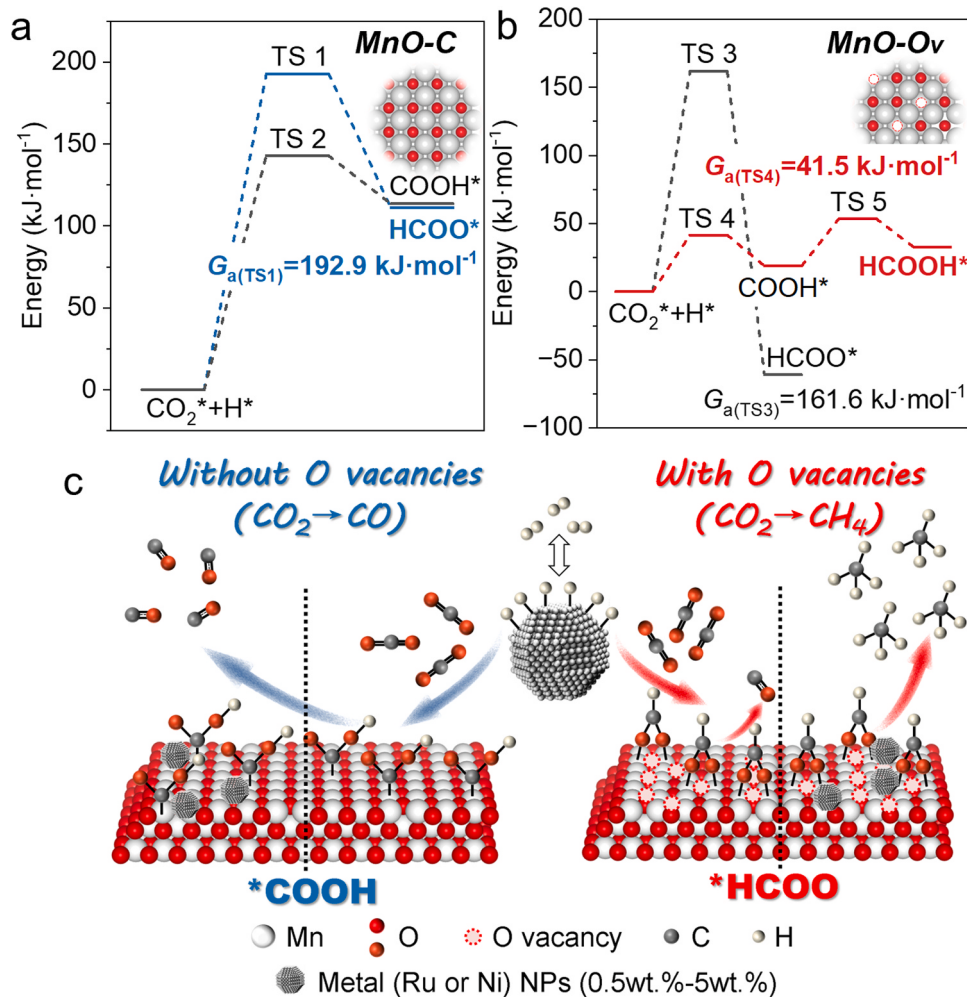


Fig. 5. The energy barrier for the formation of COOH and HCOO (or HCOOH) species over (a) MnO-C and (b) MnO-O_v. (c) The scheme of the catalytic pathway for the CO_2 hydrogenation over RuMn-C and RuMn-O_v.

recorded for both RuMn-C (0.5 wt% of Ru) and 5%RuMn-C (5 wt% of Ru) suggested that the surface oxygen vacancy density has a greater influence on H spillover than the amount of Ru metal [57]. Consequently, the stronger H spillover also contributed to the higher methanation activity and selectivity [55]. As mentioned above, the CH_4 selectivity of RuMn-O_v catalyst increased with the increased $\text{H}_2:\text{CO}_2$ ratio and Ru loading. On the contrary, the same factors do not influence the selectivity in RuMn-C.

These results demonstrate the importance of formate formation and efficient dissociation of H_2 for CH_4 generation. Our previous research concerning MnO-based catalysts illustrated that the augmentation of H-spillover does not foster methane production in the absence of formate formation [36].

In summary, MnO_x-O_v support has a significantly higher amount of surface oxygen vacancies than MnO_x-C support, resulting in an enhanced CO_2 adsorption ability and a higher intrinsic reactivity of formate intermediates during CO_2 hydrogenation (Fig. 5c). The role of Ru nanoparticles is to generate spillover H, while it does not directly participate in the reaction mechanism. The surface oxygen vacancies favour a faster spillover hydrogen diffusion, thus determining the selectivity of methane from this perspective. Through the adsorption of CO_2 at the surface, Brønsted sites nearby oxygen vacancies, a chemisorbed CO_2 species characterised by an enhanced O-C-O asymmetric bending of formate (due to the presence of spillover H) forms, then converted to methane. Therefore, the selectivity of CO_2 hydrogenation is governed by the interplay between support-dependent formate

formation and metal-dependent H_2 dissociation. Theoretical modelling further supports these results and the type of species formed in the reaction mechanism.

4. Conclusion

Two kinds of RuMn catalysts, RuMn-O_v and RuMn-C, were successfully synthesised, with the sole difference being the surface oxygen vacancy content. The RuMn-O_v catalyst demonstrates a pronounced CH_4 selectivity within the temperature range 320–500 °C, whereas RuMn-C exhibits nearly 100 % CO selectivity. The variation in selectivity is not attributable to differences in metal properties (such as electronic state, particle size, and the strong metal-support interaction effect) or the metal's CO hydrogenation ability. *In-situ* DRIFTS studies revealed that formate intermediates are generated on the surface of the high-defective RuMn-O_v catalyst while not on the low-defective RuMn-C catalyst. Furthermore, the formate intermediates efficiently hydrogenate into methane with spillover H from metal Ru. Previous studies have overly emphasised the impact of metal or metal/support interface properties on catalytic selectivity, often neglecting the significance of the support itself in the selective generation of intermediates.

The novel aspects proven by these results, supported by extended characterisation results, *in-situ* mechanistic data and theoretical modelling, are that in our catalysts, 1) the support plays the decisive role in triggering selectivity and activity, with Ru nanoparticles only acting to generate spillover H, which then diffuses to the active sites on the

MnO_x support, and 2) surface oxygen vacancies on MnO_x induces the generation of the formate, key intermediate in the surface path to methane. The surface oxygen vacancies also facilitate H spillover transport and thus promote activity.

Building upon this novel insight, we have, for the first time, achieved a high CO selectivity under a Ru loading content of up to 5 wt% on the RuMn-C catalyst. These findings provide a comprehensive understanding of the mechanism underlying the atmospheric and even pressurized CO_2 hydrogenation reaction and serve as a crucial foundation for designing highly selective catalysts.

Data availability

Data will be made available on request.

CRediT authorship contribution statement

Hui Kang: Writing – original draft, Visualization, Validation, Software, Formal analysis, Data curation, Conceptualization. **Lixuan Ma:** Resources, Formal analysis, Data curation. **Shiyan Li:** Resources, Investigation, Data curation. **Wei Chu:** Writing – review & editing, Visualization, Validation, Supervision, Conceptualization. **Riguang Zhang:** Writing – original draft, Supervision, Resources, Methodology. **Siglinda Perathoner:** Writing – review & editing, Visualization. **Gabriele Centi:** Writing – review & editing, Visualization, Methodology, Conceptualization. **Yuefeng Liu:** Writing – review & editing, Supervision, Project administration, Funding acquisition, Conceptualization.

Declaration of Competing Interest

The authors declare that they have no known competing financial interests or personal relationships that could have appeared to influence the work reported in this paper.

Data availability

Data will be made available on request.

Acknowledgements

This work was financially supported by the NSFC of China (Nos. 22172161, 22102147, U23A20132 and 21972140), LiaoNing Revitalization Talents Program (XLYC1907053), Dalian Institute of Chemical Physics (DICP I202421) and the AI S&T Program of Yulin Branch, Dalian National Laboratory for Clean Energy, CAS (DNL-YLA202204). S.P. and G.C. also thank the support from the CAS President's International Fellowship Initiative (PIFI) program and the SCOPE ERC Synergy Project (ID 810182).

Appendix A. Supporting information

Supplementary data associated with this article can be found in the online version at [doi:10.1016/j.apcatb.2024.124010](https://doi.org/10.1016/j.apcatb.2024.124010).

References

- [1] A. Velty, A. Corma, Advanced zeolite and ordered mesoporous silica-based catalysts for the conversion of CO_2 to chemicals and fuels, *Chem. Soc. Rev.* 52 (2023) 1773–1946.
- [2] H. Kang, J. Ma, S. Perathoner, W. Chu, G. Centi, Y. Liu, Understanding the complexity in bridging thermal and electrocatalytic methanation of CO_2 , *Chem. Soc. Rev.* 52 (2023) 3627–3662.
- [3] M.D. Porosoff, B.H. Yan, J.G.G. Chen, Catalytic reduction of CO_2 by H_2 for synthesis of CO, methanol and hydrocarbons: challenges and opportunities, *Energy Environ. Sci.* 9 (2016) 62–73.
- [4] S. Li, Y.X. Xu, H.W. Wang, B.T. Teng, Q. Liu, Q.H. Li, L.L. Xu, X.Y. Liu, J.L. Lu, Tuning the CO_2 hydrogenation selectivity of rhodium single-atom catalysts on zirconium dioxide with alkali ions, *Angew. Chem. Int. Ed.* 135 (8) (2023) e202218167.
- [5] J.F. Simons, T.J. de Heer, R.C. van de Poll, V. Muravev, N. Kosinov, E.J. Hensen, Structure sensitivity of CO_2 hydrogenation on Ni revisited, *J. Am. Chem. Soc.* 145 (2023) 20289–20301.
- [6] J. Ma, Q. Jiang, Y. Zhou, W. Chu, S. Perathoner, C. Jiang, K.H. Wu, G. Centi, Y. Liu, Tuning the chemical properties of $\text{Co}-\text{Ti}_3\text{C}_2\text{T}_x$ MXene materials for catalytic CO_2 reduction, *Small* 17 (2021) 2007509.
- [7] S. Kattel, P. Liu, J.G. Chen, Tuning selectivity of CO_2 hydrogenation reactions at the metal/oxide interface, *J. Am. Chem. Soc.* 139 (2017) 9739–9754.
- [8] X.Y. Li, J. Lin, L. Li, Y.K. Huang, X.L. Pan, S.E. Collins, Y.J. Ren, Y. Su, L.L. Kang, X. Y. Liu, Y.L. Zhou, H. Wang, A.Q. Wang, B.T. Qiao, X.D. Wang, T. Zhang, Controlling CO_2 hydrogenation selectivity by metal-supported electron transfer, *Angew. Chem. Int. Ed.* 59 (2020) 19983–19989.
- [9] A. Aitbekova, L.H. Wu, C.J. Wrasman, A. Boubnov, A.S. Hoffman, E.D. Goodman, S. R. Bare, M. Cargnello, Low-temperature restructuring of CeO_2 -supported Ru nanoparticles determines selectivity in CO_2 catalytic reduction, *J. Am. Chem. Soc.* 140 (2018) 13736–13745.
- [10] Y. Ma, Y. Ren, Y. Zhou, W. Liu, W. Baaziz, O. Ersen, C. Pham-Huu, M. Greiner, W. Chu, A. Wang, High-density and thermally stable palladium single-atom catalysts for chemoselective hydrogenations, *Angew. Chem. Int. Ed.* 132 (2020) 21797–21803.
- [11] H. Xin, L. Lin, R. Li, D. Li, T. Song, R. Mu, Q. Fu, X. Bao, Overturning CO_2 hydrogenation selectivity with high activity via reaction-induced strong metal-support interactions, *J. Am. Chem. Soc.* 144 (2022) 4874–4882.
- [12] M.D. Porosoff, J.G.G. Chen, Trends in the catalytic reduction of CO_2 by hydrogen over supported monometallic and bimetallic catalysts, *J. Catal.* 301 (2013) 30–37.
- [13] A. Solis-Garcia, T.A. Zepeda, J.C. Fierro-Gonzalez, Spectroscopic evidence of the simultaneous participation of rhodium carbonyls and surface formate species during the CO_2 methanation catalyzed by ZrO_2 -supported Rh, *Appl. Catal. B* 304 (2022) 120955.
- [14] F. Wang, S. He, H. Chen, B. Wang, L.R. Zheng, M. Wei, D.G. Evans, X. Duan, Active site dependent reaction mechanism over Ru/ CeO_2 catalyst toward CO_2 methanation, *J. Am. Chem. Soc.* 138 (2016) 6298–6305.
- [15] L.F. Bobadilla, J.L. Santos, S. Ivanova, J.A. Odriozola, A. Urakawa, Unravelling the role of oxygen vacancies in the mechanism of the reverse water-gas shift reaction by operando DRIFTS and ultraviolet-visible spectroscopy, *ACS Catal.* 8 (2018) 7455–7467.
- [16] A.I. Rabee, D. Zhao, S. Cisneros, C.R. Kreyenschulte, V. Kondratenko, S. Bartling, C. Kubis, E.V. Kondratenko, A. Brückner, J. Rabeh, Role of interfacial oxygen vacancies in low-loaded Au-based catalysts for the low-temperature reverse water-gas shift reaction, *Appl. Catal. B* 321 (2023) 122083.
- [17] Z. Feng, C. Tang, P. Zhang, K. Li, G. Li, J. Wang, Z. Feng, C. Li, Asymmetric sites on the ZnZrO_x catalyst for promoting formate formation and transformation in CO_2 hydrogenation, *J. Am. Chem. Soc.* 145 (2023) 12663–12672.
- [18] N.H.M. Dostagir, R. Rattanawan, M. Gao, J. Ota, J.-y. Hasegawa, K. Asakura, A. Fukouka, A. Shrotri, Co single atoms in ZrO_2 with inherent oxygen vacancies for selective hydrogenation of CO_2 to CO, *ACS Catal.* 11 (2021) 9450–9461.
- [19] H. Zheng, W. Liao, J. Ding, F. Xu, A. Jia, W. Huang, Z. Zhang, Unveiling the key factors in determining the activity and selectivity of CO_2 hydrogenation over Ni/ CeO_2 catalysts, *ACS Catal.* 12 (2022) 15451–15462.
- [20] J. Chen, C. Chen, M. Qin, B. Li, B. Lin, Q. Mao, H. Yang, B. Liu, Y. Wang, Reversible hydrogen spillover in Ru- WO_3 enhances hydrogen evolution activity in neutral pH water splitting, *Nat. Commun.* 13 (2022) 5382.
- [21] A. Bruij, J.A. Rodriguez, P.J. Ramirez, S.D. Senanayake, J. Evans, J.B. Park, D. Stacchiola, P. Liu, J. Hrbek, F. Illas, A new type of strong metal-support interaction and the production of H_2 through the transformation of water on Pt/ CeO_2 (111) and Pt/ $\text{CeO}_2/\text{TiO}_2$ (110) catalysts, *J. Am. Chem. Soc.* 134 (2012) 8968–8974.
- [22] Y.H. Zou, W. Zhang, N. Chen, S. Chen, W.J. Xu, R.S. Cai, C.L. Brown, D.J. Yang, X. D. Yao, Generating oxygen vacancies in MnO hexagonal sheets for ultralong life lithium storage with high capacity, *ACS Nano* 13 (2019) 2062–2071.
- [23] W.L. Vrijburg, E. Moioli, W. Chen, M. Zhang, B.J. Terlingen, B. Zijlstra, I.A. Filot, A. Züttel, E.A. Pidko, E.J. Hensen, Efficient base-metal NiMn/ TiO_2 catalyst for CO_2 methanation, *ACS Catal.* 9 (2019) 7823–7839.
- [24] J. Li, Y. Zhou, X. Xiao, W. Wang, N. Wang, W. Qian, W. Chu, Regulation of Ni-CNT interaction on Mn-promoted nickel nanocatalysts supported on oxygenated CNTs for CO_2 selective hydrogenation, *ACS Appl. Mater. Interfaces* 10 (2018) 41224–41236.
- [25] Y.L. He, K.R. Yang, Z.W. Yu, Z.S. Fishman, L.A. Achola, Z.M. Tobin, J.A. Heinlein, S. Hu, S.L. Suib, V.S. Batista, L.D. Pfefferle, Catalytic manganese oxide nanostructures for the reverse water gas shift reaction, *Nanoscale* 11 (2019) 16677–16688.
- [26] J. Li, W. Li, L. Wei, R.T. Yang, Novel Y_2O_3 doped MnO_x binary metal oxides for NO_x storage at low temperature in lean burn condition, *Catal. Lett.* 129 (2009) 104–110.
- [27] V. Wang, N. Xu, J.-C. Liu, G. Tang, W.-T. Geng, VASPKIT: a user-friendly interface facilitating high-throughput computing and analysis using VASP code, *Comput. Phys. Commun.* 267 (2021) 108033.
- [28] A. Kumar, M. Kumar, R.P. Singh, Study on electronic, magnetic, optical and thermoelectric properties of manganese oxide (MnO): DFT based spin polarized calculations, *Optik* 241 (2021) 167064.
- [29] S.K. Nayak, P. Jena, Equilibrium geometry, stability, and magnetic properties of small MnO clusters, *J. Am. Chem. Soc.* 121 (1999) 644–652.
- [30] H. Yao, M. Shelef, The surface interaction of O_2 and NO with manganous oxide, *J. Catal.* 31 (1973) 377–383.

[31] E.S. Ilton, J.E. Post, P.J. Heaney, F.T. Ling, S.N. Kerisit, XPS determination of Mn oxidation states in Mn (hydr)oxides, *Appl. Surf. Sci.* 366 (2016) 475–485.

[32] A.J. Logsdail, C.A. Downing, T.W. Keal, P. Sherwood, A.A. Sokol, C.R.A. Catlow, Hybrid-DFT modeling of lattice and surface vacancies in MnO, *J. Phys. Chem. C.* 123 (2019) 8133–8144.

[33] Y. Piao, Q. Jiang, H. Li, H. Matsumoto, J. Liang, W. Liu, C. Pham-Huu, Y. Liu, F. Wang, Identify Zr promotion effects in atomic scale for co-based catalysts in Fischer–Tropsch synthesis, *ACS Catal.* 10 (2020) 7894–7906.

[34] N.C. Nelson, L. Chen, D. Meira, L. Kovarik, J. Szanyi, In situ dispersion of palladium on TiO₂ during reverse water-gas shift reaction: formation of atomically dispersed palladium, *Angew. Chem. Int. Ed.* 59 (2020) 17657–17663.

[35] E.I. Koitsoumpa, S. Karella, Equilibrium and kinetic aspects for catalytic methanation focusing on CO₂ derived substitute natural gas (SNG), *Renew. Sust. Energ. Rev.* 94 (2018) 536–550.

[36] H. Kang, L. Zhu, S. Li, S. Yu, Y. Niu, B. Zhang, W. Chu, X. Liu, S. Perathoner, G. Centi, Y. Liu, Generation of oxide surface patches promoting H-spillover in Ru/TiO₂/MnO catalysts enables CO₂ reduction to CO, *Nat. Catal.* 6 (2023) 1062–1072.

[37] E. Loccufier, G. Watson, Y.R. Zhao, M. Meledina, R. Denis, P.G. Derakhshandeh, P. V. Voort, K. Leus, D.P. Debecker, K. De Buysser, K. De Clerck, CO₂ methanation with Ru@MIL-101 nanoparticles fixated on silica nanofibrous veils as stand-alone structured catalytic carrier, *Appl. Catal. B* 320 (2023) 121972.

[38] R.C. Rabelo-Neto, M.P. Almeida, E.B. Silveira, M. Ayala, C.D. Watson, J. Villarreal, D.C. Cronauer, A.J. Kropf, M. Martinelli, F.B. Noronha, G. Jacobs, CO₂ hydrogenation: Selectivity control of CO versus CH₄ achieved using Na doping over Ru/m-ZrO₂ at low pressure, *Appl. Catal. B* 315 (2022) 121533.

[39] J. Dou, Y. Sheng, C. Choong, L.W. Chen, H.C. Zeng, Silica nanowires encapsulated Ru nanoparticles as stable nanocatalysts for selective hydrogenation of CO₂ to CO, *Appl. Catal. B* 219 (2017) 580–591.

[40] A. Cherevotan, B. Ray, S.R. Churipard, K. Kaur, U.K. Gautam, C.P. Vinod, S. C. Peter, Influence of support textural property on CO₂ to methane activity of Ni/SiO₂ catalysts, *Appl. Catal. B* 317 (2022) 121692.

[41] S. Cao, Y. Ma, W. Chu, Y.F. Liu, High-density MoC_x nanoclusters anchored on nanodiamond-derived nanocarbon as a robust CO₂ reduction catalyst for syngas production, *Fuel* 323 (2022) 124347.

[42] J.H. Kwak, L. Kovarik, J. Szanyi, CO₂ reduction on supported Ru/Al₂O₃ catalysts: cluster size dependence of product selectivity, *ACS Catal.* 3 (2013) 2449–2455.

[43] S. Sharma, Z.P. Hu, P. Zhang, E.W. McFarland, H. Metiu, CO₂ methanation on Ru-doped ceria, *J. Catal.* 278 (2011) 297–309.

[44] C. Vogt, E. Groeneveld, G. Kamsma, M. Nachtegaal, L. Lu, C.J. Kiely, P.H. Berben, F. Meirer, B.M. Weckhuysen, Unravelling structure sensitivity in CO₂ hydrogenation over nickel, *Nat. Catal.* 1 (2018) 127–134.

[45] S.W. Li, Y. Xu, Y.F. Chen, W.Z. Li, L.L. Lin, M.Z. Li, Y.C. Deng, X.P. Wang, B.H. Ge, C. Yang, S.Y. Yao, J.L. Xie, Y.W. Li, X. Liu, D. Ma, Tuning the selectivity of catalytic carbon dioxide hydrogenation over iridium/cerium oxide catalysts with a strong metal-support interaction, *Angew. Chem. Int. Ed.* 56 (2017) 10761–10765.

[46] X. Yuan, T. Pu, M. Gu, M. Zhu, J. Xu, Strong metal-support interactions between nickel and iron oxide during CO₂ hydrogenation, *ACS Catal.* 11 (2021) 11966–11972.

[47] J.C. Matsubu, S.Y. Zhang, L. DeRita, N.S. Marinkovic, J.G.G. Chen, G.W. Graham, X.Q. Pan, P. Christopher, Adsorbate-mediated strong metal-support interactions in oxide-supported Rh catalysts, *Nat. Chem.* 9 (2017) 120–127.

[48] Y. Guo, S. Mei, K. Yuan, D.J. Wang, H.C. Liu, C.H. Yan, Y.W. Zhang, Low-temperature CO₂ methanation over CeO₂-supported Ru single atoms, nanoclusters, and nanoparticles competitively tuned by strong metal-support interactions and H-spillover effect, *ACS Catal.* 8 (2018) 6203–6215.

[49] N.C. Nelson, M.-T. Nguyen, V.-A. Glezakou, R. Rousseau, J. Szanyi, Carboxyl intermediate formation via an in situ-generated metastable active site during water-gas shift catalysis, *Nat. Catal.* 2 (2019) 916–924.

[50] W.H. Li, G.H. Zhang, X. Jiang, Y. Liu, J. Zhu, F.S. Ding, Z.M. Liu, X.W. Guo, C. S. Song, CO₂ hydrogenation on unpromoted and M-promoted Co/TiO₂ catalysts (M = Zr, K, Cs): effects of crystal phase of supports and metal-support interaction on tuning product distribution, *ACS Catal.* 9 (2019) 2739–2751.

[51] J. Ye, C. Liu, D. Mei, Q. Ge, Active oxygen vacancy site for methanol synthesis from CO₂ hydrogenation on In₂O₃(110): a DFT study, *ACS Catal.* 3 (2013) 1296–1306.

[52] T.F. Zhang, W.W. Wang, F.N. Gu, W.Q. Xu, J.L. Zhang, Z.X. Li, T.Y. Zhu, G.W. Xu, Z.Y. Zhong, F.B. Su, Enhancing the low-temperature CO₂ methanation over Ni/La-CeO₂ catalyst: The effects of surface oxygen vacancy and basic site on the catalytic performance, *Appl. Catal. B* 312 (2022) 121385.

[53] G. Yang, H. Zhao, X. Luo, K. Shi, H. Zhao, W. Wang, Q. Chen, H. Fan, T. Wu, Promotion effect and mechanism of the addition of Mo on the enhanced low-temperature SCR of NO_x over MnO_x/gamma-Al₂O₃ Catalysts, *Appl. Catal. B* 245 (2019) 743–752.

[54] F.C. Meunier, I. Dansette, A. Paredes-Nunez, Y. Schuurman, Cu-Bound formates are main reaction intermediates during CO₂ hydrogenation to methanol over Cu/ZrO₂, *Angew. Chem. Int. Ed.* 62 (2023) e202303939.

[55] C.T. Wang, E. Guan, L. Wang, X.F. Chu, Z.Y. Wu, J. Zhang, Z.Y. Yang, Y.W. Jiang, L. Zhang, X.J. Meng, B.C. Gates, F.S. Xiao, Product selectivity controlled by nanoporous environments in zeolite crystals enveloping rhodium nanoparticle catalysts for CO₂ hydrogenation, *J. Am. Chem. Soc.* 141 (2019) 8482–8488.

[56] A. Mahdavi-Shakib, T.N. Whittaker, T.Y. Yun, K.B. Sravan Kumar, L.C. Rich, S. Wang, R.M. Rioux, L.C. Grabow, B.D. Chandler, The role of surface hydroxyls in the entropy-driven adsorption and spillover of H₂ on Au/TiO₂ catalysts, *Nat. Catal.* 6 (2023) 710–719.

[57] H.Y.T. Chen, S. Tosoni, G. Pacchioni, Hydrogen adsorption, dissociation, and spillover on Ru-10 clusters supported on anatase TiO₂ and tetragonal ZrO₂ (101) surfaces, *ACS Catal.* 5 (2015) 5486–5495.